DISCLAIMER

LLNL-TR-2002096

Lawrence Livermore National Laboratory

Prediction and Analysis of Utah FORGE Injection Activities using a Coupled Thermo-hydro-mechanical and Earthquake (THM+E) Modeling

F. Fei, C. Wang, K. Kroll Whiteside

February 2025

PREDICTION AND ANALYSIS OF UTAH FORGE INJECTION ACTIVITIES USING A COUPLED THERMO-HYDRO-MECHANICAL AND EARTHQUAKE (THM+E) MODELING WORKFLOW

Organization:	University of Utah
Recipient Organization:	Lawrence Livermore National Laboratory
DUNS Number:	009095365
Recipient Address:	7000 East Ave. Livermore, CA 94550

Award Number:	5-2428
Project Title:	Coupled investigation of fracture permeability impact on reservoir stress and seismic
Project Period:	January 1, 2024 to December 31, 2024

Principal Investigator(s):	Kayla Kroll (PI) krollwhitesi1@llnl.gov
Report prepared by:	Fan Fei (LLNL) Chaoyi Wang (LLNL) Kayla Kroll (LLNL)
Report Submitted by:	Kayla Kroll

Date of Report Submission:	March 24, 2025
Related milestones:	MILESTONE 4.1.2

This work was performed under the auspices of the U.S. Department of Energy by Lawrence Livermore National Laboratory under Contract DE-AC52-07NA27344.

1 Introduction

A coupled thermo-hydro-mechanical (THM) numerical workflow that is capable of modeling seismic slip is critical for the successful development of enhanced geothermal systems (EGS). By integrating key physical processes, this workflow enables accurate simulation of temperature and pressure diffusions, stress changes, and induced seismicity. As a result, it serves as a vital tool for predicting induced seismicity and optimizing reservoir stimulation strategies.

The Utah FORGE (Frontier Observatory for Research in Geothermal Energy) project, located near Milford, Utah, is a U.S. Department of Energy initiative aimed at advancing EGS technology. In April 2024, eight new stimulation stages (Stages 3R-10) were conducted in well 16A (injection well) subsequent to the first series of stimulation (Stages 1-3) performed in April, 2022. To monitor the induced seismicity, geophones were deployed in wells 58-32, 56-32, and 78B-32, while fiber optic cables were also installed in wells 16B, 78-32, and 78B-32 to collect microseismic data and detect frac hits Preliminary analyses of microseismic catalogs and fiber optic data suggest that the stimulated fractures in Stages 3R–6 closely align with that generated during Stage 3, indicating that the new stimulations were likely reactivating the previously stimulated fracture. To better understand the underlying process, a comprehensive modeling approach that can accurately capture thermal, hydrological, mechanical, and seismic responses is essential.

In this work, we propose and utilize a coupled thermo-hydro-mechanical and earthquake (THM+E) simulation workflow to numerically investigate the stimulation activities on well 16A. The specific objective is to confirm whether the new stimulation stages (Stages 3R–6) reactivated fractures previously stimulated during Stage 3. For this purpose, we perform THM+E simulations individually for Stages 3, 3R, 4, and 5, incorporating the discrete fracture networks (DFNs) created by the plane-fitting technique based on the microseismic catalogs. The simulation workflow consists of two separate models: a THM model and an earthquake model, coupled in a one-way manner. Detailed descriptions of the workflow are provided in Section 3. Simulation results are presented in terms of injection pressure, permeability evolution, and predicted seismic catalogs, which are then compared with field data for further analyses.

This report is structured as follows. In Section 2, we present detailed analyses of the field data and propose the hypothesis that the new stimulation stages (Stages 3R–6) were probably reactivating the previously stimulated fractures in Stage 3. In Section 3, we introduce the coupled THM+E workflow and the problem setup to validate our hypothesis, followed by the simulation results for each stage in Section 4. Meanwhile, discussions are included to analyze the model predictions and their comparison with field data. Lastly, we conclude the report and outline

future plans in Section 5.

2 Utah FORGE Field Stimulations

In this section, we show the analysis of field data from stimulation activities conducted on the 16(A)78-32 Well, with a focus on the available microseismic and fiber optic data. The analysis implies that the new stimulation stages (Stages 3R–6) were probably *reactivating* the previously stimulated fractures in Stage 3, rather than creating new fractures. Details of the analysis are provided below.

2.1 Microseismic data analysis

We start by analyzing microseismic data recorded during the stimulation period of the 16(A)78-32 Well. Figure 1 illustrates the microseismic events from all stimulation stages conducted in 2024 (*i.e.,* Stages 3R-10), along with those from 2022 (*i.e.,* Stage 3).

With these microseismic catalogs, we use principal component analysis (PCA) technique to perform plane-fitting for each stimulation stage, PCA is a standard technique used to perform unsupervised clustering for data, the method extracts the direction where the data have the most spatial variance and fits a circular plane to that direction. Details of the PCA technique are well documented in other literature and are omitted here for brevity.

As shown in Figure 2, the plane fitting results indicate that the fracture planes for Stages 3-6 are closely aligned and intersecting. This observation, implies the possibility that Stages 3 to 6 stimulated the same fracture or a fractured zone. Therefore, we hypothesize that a fracture or a fracture system was originally generated in Stage 3, with subsequent Stages 3R-6 reactivating and expanding the same fracture or fracture system.

We plotted the microseismic catalogs of Stages 3–6 on a distance-time or radius-time (RT) graph (Figure.3), the RT graph provides visual estimates of how fast the fluid pressure front moves away from the stimulation location. In Figure.3, Stage 3 microseismic (red circles) events clearly show a gradual increase in distance from the origin over time, this move out pattern matches the expected microseismic behavior of a propagating fracture. Stage 3R and beyond happened one year later than Stage 3, therefore, for better visualization, we plot the microseismic events from Stages 3R to 6 right after Stage 3. For Stages 3R to 6, there are much less microseismic events compared to Stage 3. The move out patterns are not clearly observed as some microseismic events far from the injection occur almost at the same time with the closer events. This observation suggests that Stages 3R to 6 was reactivating the fracture from Stage 3,

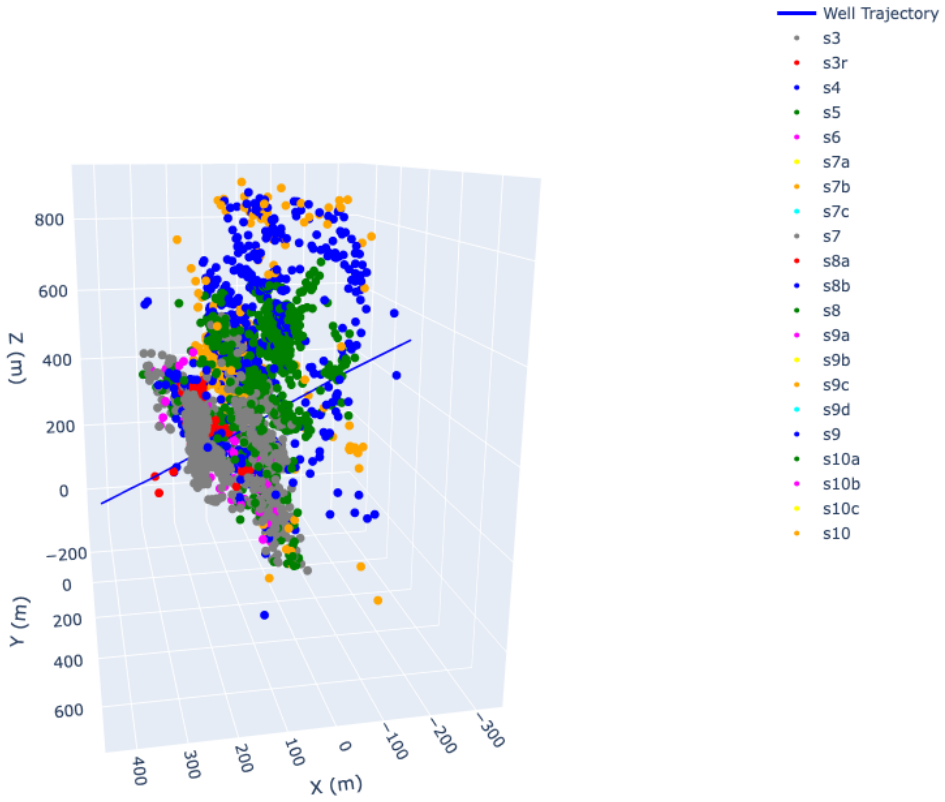

Figure 1: Microseismic events from stimulation Stages 3-10 on the 16(A)78-32 Well (blue).

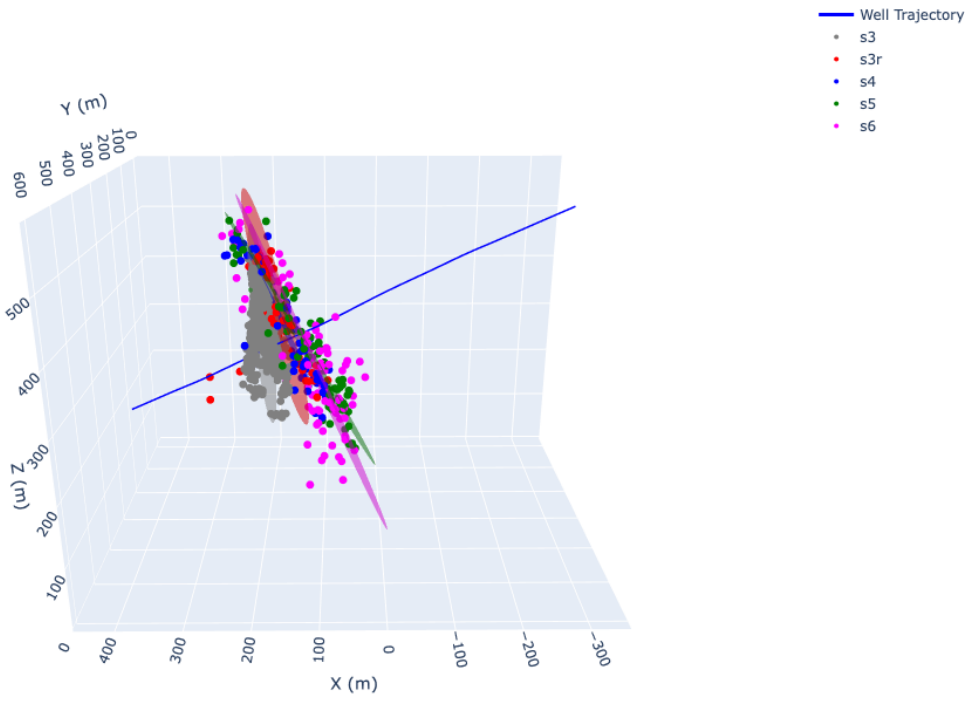

Figure 2: Fitted fracture planes for Stages 3-6 based on their microseismic catalogues.

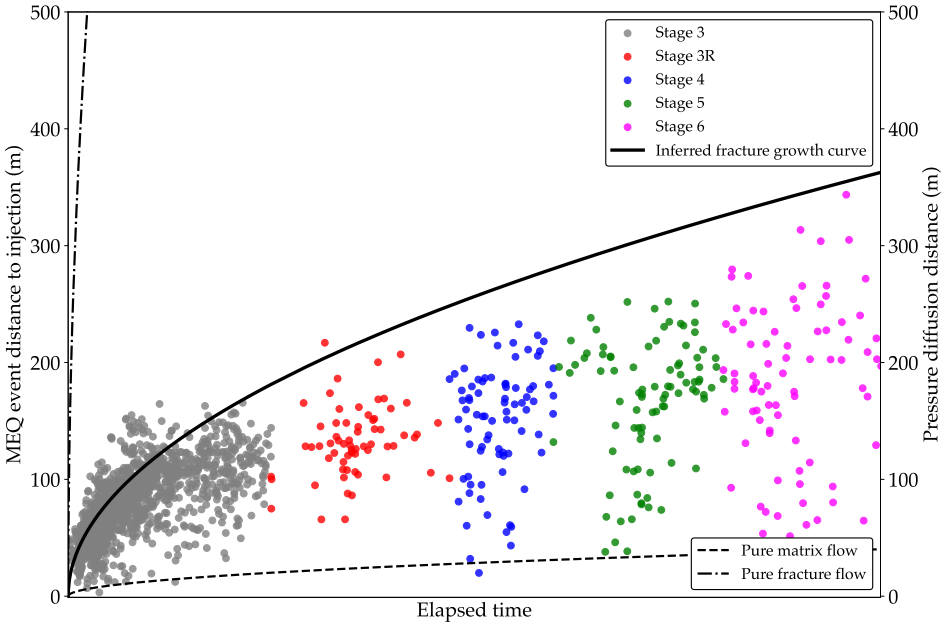

Figure 3: Distance-time plots for microseismic events of Stages 3-6, along with two pressure diffusion curves representing the flow in matrix and fracture, respectively. Note: the time axis is not scaled to real time. Events of all stages are combined by linking the last event of one stage to the first event of the next.

so that the pressure front can travel instantaneously to the edge for these subsequent stages.

We fitted a RT curve for all microseismic events from Stage 3 to 6 (solid curve in Figure 3) using a volumetric expansion formulation for stimulated fractures (Haffener et al., 2022). The slope of the RT curves represent the speed of pressure front. We plot two additional curves representing the scenarios where fluid pressure front moves through the reservoir matrix by diffusion, *i.e.,* , the slowest scenario (dashed curve in Figure.3), and moves through an open fracture by advection, *i.e.,* , the fastest scenario (dotted dash curve in Figure.3). The slope of the fitted RT curve lies between the fracture matrix diffusion curve and the advection curve, suggesting the pressure front represents stimulation of the same fracture plane. Furthermore, the microseismic events from Stages 3R to 6 are capped by the same RT curve, implying they all originated from the same fracture plane or fracture zone (Kroll et al., 2017).

Our analysis show that our hypothesis is probably reflecting what happened in the field, *i.e.,* Stages 3R-6 were reactivating the same fracture or fracture zones created by Stage 3.

2.2 Fiber optic data interpretation

The fiber optic data collected during the stimulation also supports the hypothesis. Figure 4 shows a waterfall plot of the strain change along the fiber optic cable installed on the 16(B)-78-32 Well

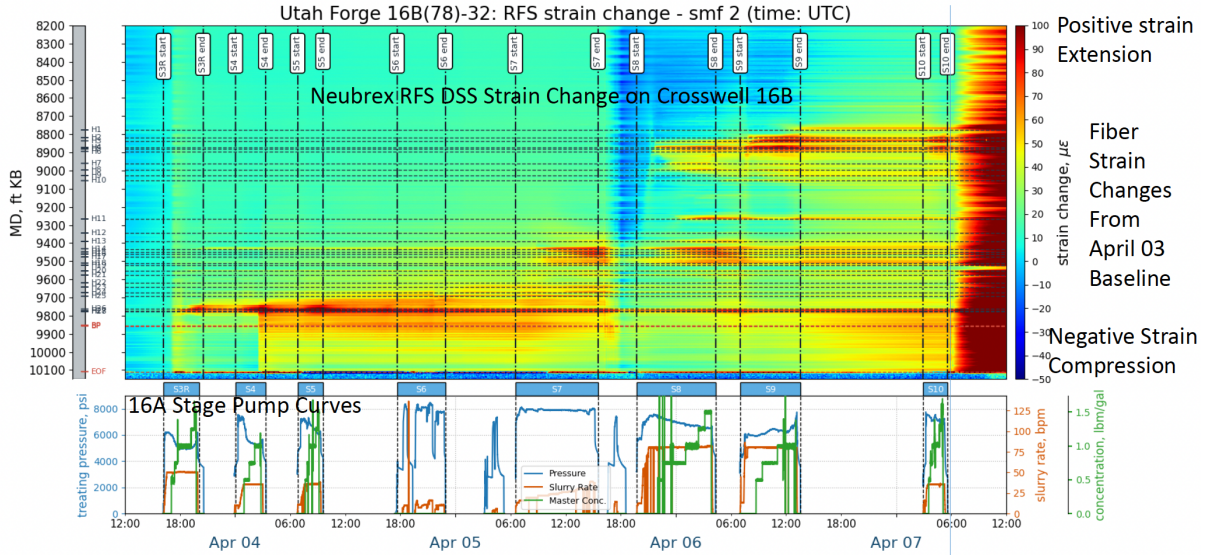

Figure 4: RFS DSS strain change from the fiber optic cable installed on the 16B(78)-32 Well. Figure directly captured from Jurick et al. (2024).

during new stimulation stages in 2024 (Jurick et al., 2024). A pointy red strip is clearly visible around 9800 feet MD immediately after Stage 3R begins. Typically, a new fracture will show a red heart-shaped pattern on the waterfall plot when interacting with the fiber optic cable (Jin & Roy, 2017; Wang et al., 2023), because of an advancing "process zone" for a propagating fracture. A pointy strip without apparent heart-shaped pattern indicats the re-opening of an existing fracture (Haffener et al., 2022).

The red strip signal persists throughout Stages 3R–6 at the same location, no additional signals were observed during the same stimulation period. Diffusive red patterns also appear below the main signal close to the end of Stage 4, but the main signal initiated in Stage 3R remained the dominant feature. The data interpretation provides strong evidence that Stages 3R–6 reopened the same fracture plane around 9800 feet MD of the 16(B)78-32 Well, which supports the hypothesis in the previous section.

3 Coupled THM+E Simulation: Workflow and Model Setup

In this section, we demonstrate a coupled thermo-hydro-mechanical and earthquake (THM+E) simulation workflow to numerically investigate our hypothesis that Stages 3R–6 were essentially reactivating the previously stimulated region generated during Stage 3, rather than initiating new

fractures.

The section is structured as follows. First, we introduce the coupled workflow for the THM+E simulation and describe the problem setup. We then perform THM simulations for Stages 3–5, incorporating the DFN permeability field derived from the plane-fitting results shown in Figure 2 Note that Stage 6 is excluded from this study due to unexpected injection results obtained in the field. For each stage, we calibrate the permeability enhancement model parameters within the THM solver by history matching the pressure data to account for stimulation effects. Subsequently, the stress and pressure fields from the THM model are fed to an earthquake simulator to simulate the seismic response. The simulated earthquake catalogs are then compared with the field microseismic data to assess the validity of our hypothesis.

The workflow integrates a THM simulation with an earthquake simulation, coupled in an one-way manner through the following steps:

1. **THM simulation:** We simulate the stimulation using a geomechanics coupled reservoir model built in GEOS, a multiphysics simulator based on the coupled finite element and finite volume method. We use fully implicit THM solver to capture the THM response of the system.

2. **THM results processing:** upon completion of the THM simulation at the end of injection, we extract the time histories of stress and pressure, projecting the data on fitted fault planes.

3. **Earthquake simulation:** the stress and pressure data are then transferred to a earthquake simulator based on quasi-dynamic boundary element method, RSQSim (Richards-Dinger & Dieterich, 2012), for conducting earthquake simulations on the fault planes.

3.1 THM Modeling Set-up

The THM simulation setup with DFN permeability is presented in Figure 5, including all stages of interest in this study, *i.e.,* from Stage 3 to 5. To validate our hypothesis that new stimulation stages primarily reactivated the region stimulated during Stage 3, we design two problem setups: one for Stage 3 and another for Stages 3R–5. The only difference between these setups lies in the DFN permeability field. More specifically, the Stage 3 setup (Figure 5a) includes only those DFNs associated with Stages 1 and 2. However, the setup of Stages 3R-5 (Figure 5b) incorporates additional DFNs fitted to microseismic data of new stimulation stages, to align our assumption that these new stimulations were reactivating the pre-existing fractures. Both setups adopt the initial conditions of pressure, temperature, and in situ stresses provided in Table 1. The essential material properties used in the simulations are summarized in Table 2. To

Variable	Value at TVD=2775 m	Gradient
Pressure, p	27.04 MPa	0.00981 MPa/m
Temperature, T	194.5 °C	0.06 °C/m
Total minimum horizontal stress, σ_h	46.06 MPa	0.0132 MPa/m
Total maximum horizontal stress, σ_H	52.06 MPa	0.0132 MPa/m
Total vertical stress, σ_v	67.94 MPa	0.0195 MPa/m

Table 1: Initial conditions for the simulation.

account for permeability enhancement due to hydraulic stimulation, we employ the following pressure-dependent permeability model (Morrow & Lockner, 1994; Nathenson, 1999) to provide a first-order approximation, which has also been utilized by Lee and Ghassemi (2023) in FORGE modeling,

$$\bar{k}(p) = k_0 \exp\left[\alpha_k (p - p_0)\right], \tag{1}$$

where α_k is a pressure-dependence coefficient, p_0 indicates the initial pressure, and $k_{\max}$ is the maximum permeability that can be attained. Also, we consider an anisotropic permeability, assuming hydraulic fractures propagate in the direction normal to the x-direction (σ_h), such that permeability enhancement occurs only in y- and z-directions:

$$k_x = k_0, \;\; k_y = \max\{\bar{k}(p), k_{\max}\}, \;\; k_z = \max\{\bar{k}(p), k_{\max}\}, \tag{2}$$

where $k_{\max}$ denotes a maximum attainable permeability. In the following numerical examples, we calibrate α_k and $k_{\max}$ by history matching the observed injection pressure for each stimulation stage.

3.2 Earthquake Modeling Set-up

In this work, we employ the 3D boundary element, multicycle earthquake simulator, RSQSim (J. H. Dieterich & Richards-Dinger, 2010; Richards-Dinger & Dieterich, 2012; J. H. Dieterich et al., 2015). RSQSim uses rate- and state-dependent friction (RSF) to describe conditions that control fault slip. With RSF, earthquake nucleation occurs when fault stress conditions exceed steady-state values. The RSF constitutive relationship (H. Dieterich J., 1979; A. Ruina, 1983) is given by

$$\tau = (\sigma_0 - p)\left[\mu_0 + a \ln\left(\frac{V}{V^*}\right) + b \ln\left(\frac{\theta V^*}{D_c}\right)\right], \tag{3}$$

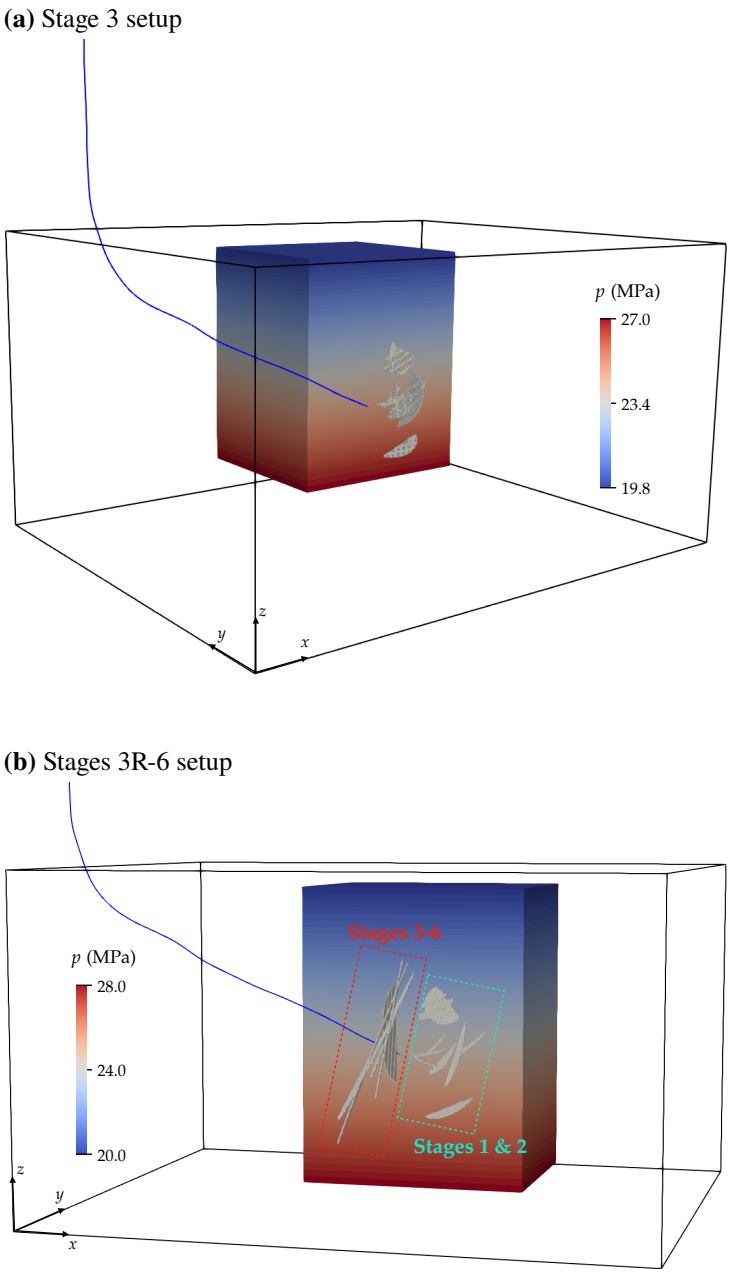

Figure 5: Overview of the problem setup with DFN permeability.

Rock matrix	**Values**	**Units**
Young's modulus, E	55	GPa
Poisson's ratio, ν	0.26	-
Biot coefficient, b	1.0	-
Reference permeability, k_0	50×10^{-18}	m^2
Initial porosity, ϕ_0	0.01	-
Thermal expansion coefficient, α_T	10^{-7}	$1/°C$
Volumetric heat capacity, C_m	2400	$kJ/K/m^3$
Thermal conductivity, k_T	4.0	W/K/m
Fluid		
Viscosity, μ_f	0.001	Pa·s
Compressibility, c_w	10^{-8}	Pa^{-1}
Specific heat capacity, C_f	4200	J/K/kg
Upscaled DFN permeability		
Initial aperture, ω_0	0.06	mm

Table 2: Material properties adopted in the THM simulation.

where a and b are the constitutive parameters that describe the material, D_c is a characteristic slip distance over which the state variable (θ) evolves, τ and σ_0 are the shear and normal stresses, μ_0 is the steady-state coefficient of friction at constant normal stress and at the reference slip speed, V^*, and V is slip speed during frictional sliding (H. Dieterich J., 1979; L. Ruina A., 1980; A. Ruina, 1983). During rupture, slip speeds in RSQSim are set by the shear impedance relation, $\dot{\delta}^{\mathrm{EQ}} = 2\beta\Delta\tau/G$ (Brune, 1970), where β is the shear wave speed, $\Delta\tau$ is the stress drop, and G is the shear modulus. The state-variable evolves by the RSF aging law (Linker & Dieterich, 1992) given by

$$\dot{\theta} = 1 - \frac{\theta V}{D_c} - \alpha \left(\frac{\theta \dot{\sigma}_{\mathrm{eff}}}{b\sigma_{\mathrm{eff}}} \right). \tag{4}$$

In the absence of tectonic loading or pore-fluid pressure perturbations, earthquakes will still nucleate if the initial shear stress (τ_0) on any element is greater than some threshold value, $\tau_{\max}$. For the size elements we use in these simulations, $\tau_{\max}$ is very close to the steady-state value (*i.e.* $\tau_{\max} \approx \tau_{\mathrm{SS}}$). At steady-state, $\theta = D_c/\dot{V}$, therefore τ_{ss} can be expressed as;

$$\tau_{\mathrm{SS}} = \sigma_0 \left[\mu_0 + (b - a) \ln \left(\frac{\theta_0 V^*}{D_c} \right) \right] \tag{5}$$

A planar fracture plane was generated at the location of the magenta plane in Figure 2 and discretized into 10 m rectangular elements. The slip vector (rake = -156.76°) was computed along this plane (with strike = 171°and dip = 69.78°) by finding the direction of maximum

traction along the planar surface in the stress field (SH_{max} = 20°). All pre-existing conditions and rate-state properties are uniform across the fracture surface, with the exception of the pre-existing shear stress conditions. This shear stress pattern on fractures arises due to heterogeneous crustal properties, geometric complexities along fault and/or fractures, and previous slip events. Here, we use a single stochastic realization based on the von Kármán (Mai & Beroza, 2002). The von Kármán auto-correlation function which has been widely used in geophysical modeling of earth systems (Goff & Jordan, 1989; Mai & Beroza, 2002; Graves & Pitarka, 2016). These type of correlated random fields are described by the power spectral density (PSD) such that,

$$PSD \propto \frac{1}{(1+k^2)^{H+1}}, \tag{6}$$

where k is the dimensionless spatial wavenumber given by $k = \sqrt{{a_x}^2{k_x}^2 + {a_y}^2{k_y}^2}$, H is the Hurst exponent, and a_x and a_y define the maximum wavelengths in the x and y direction, respectively. The field used here can be recreated based on the following parameters: H = 0.2, correlation length = 2270 m, standard deviation of the amplitude variation of 4 MPa and random seed value = 12345. All other parameters are listed in Table 3 and are based on lab experiments performed on Utah-FORGE rock in other tasks under this project.

The simulations conducted here neglect the impacts of tectonic loading, but do consider the full poroelastic stress and pore-fluid pressure changes. For this coupling, both the dynamic values of the shear and normal stresses (Equation 3) are provided by the THM simulation and projected onto a fracture surface. The pressure and stress history from all stimulations (Stage 3, 3R, 4, and 5) are concatenation and used to drive a single sinuation across all stages that preserves the time delay between Stage 3 and 3R. The distribution of the average shear stress and pore-fluid pressure projected onto the fracture surface during each stage are shown in Figures 8 and 7, respectively. The time series evolution of the maximum pore-fluid pressure on the fracture during each stage is shown in Figure 9. Note that because these simulations have been carried out to investigate the hypothesis that the only new fracture to be generated occurred during the Stage 3 stimulation and all other Stages reactive that same plane, we chose to simulate events along a *single* plane and do not consider the splay fracture that became activated following Stage 3 stimulation.

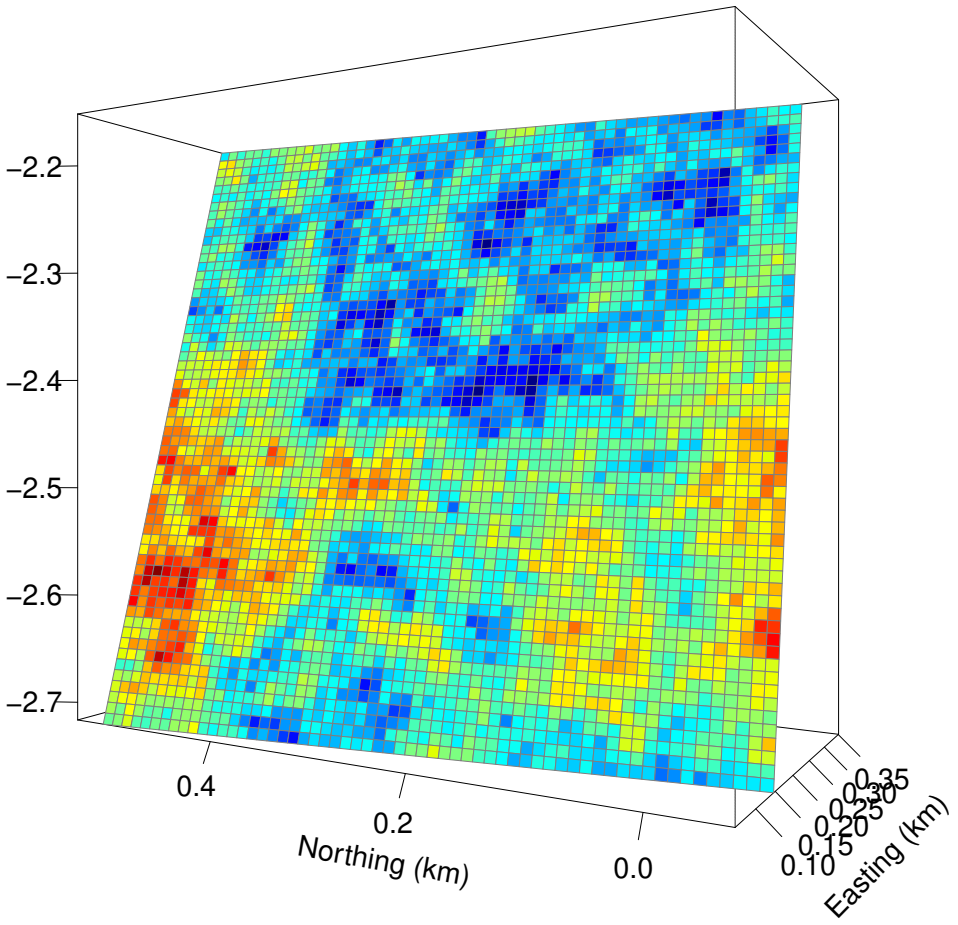

Figure 6: Visualization of the random pre-existing shear stress field used on the fracture surface at onset of the Stage 3 stimulation. The minimum (blues), maximum (reds), and average values of this distribution are 2.75 MPa, 27.85 MPa, and 14 MPa, respectively.

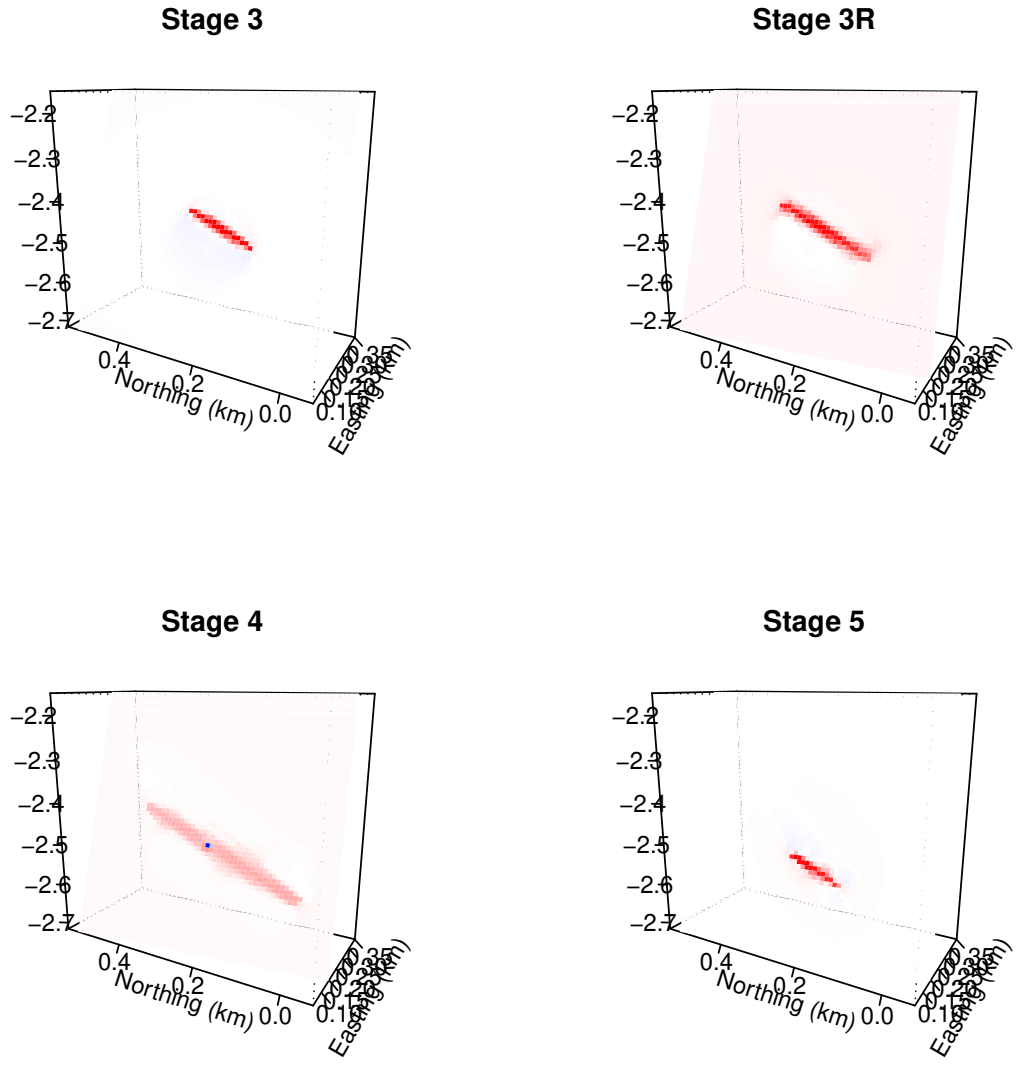

Figure 7: Visualization of the shear stress change due to each stimulation, projected onto the fracture surface at the time step that represents the average stress change across the entire stimulation. The shear stress change ranges from -4.7 MPa to 8.03 MPa across all four stimulations considered here.

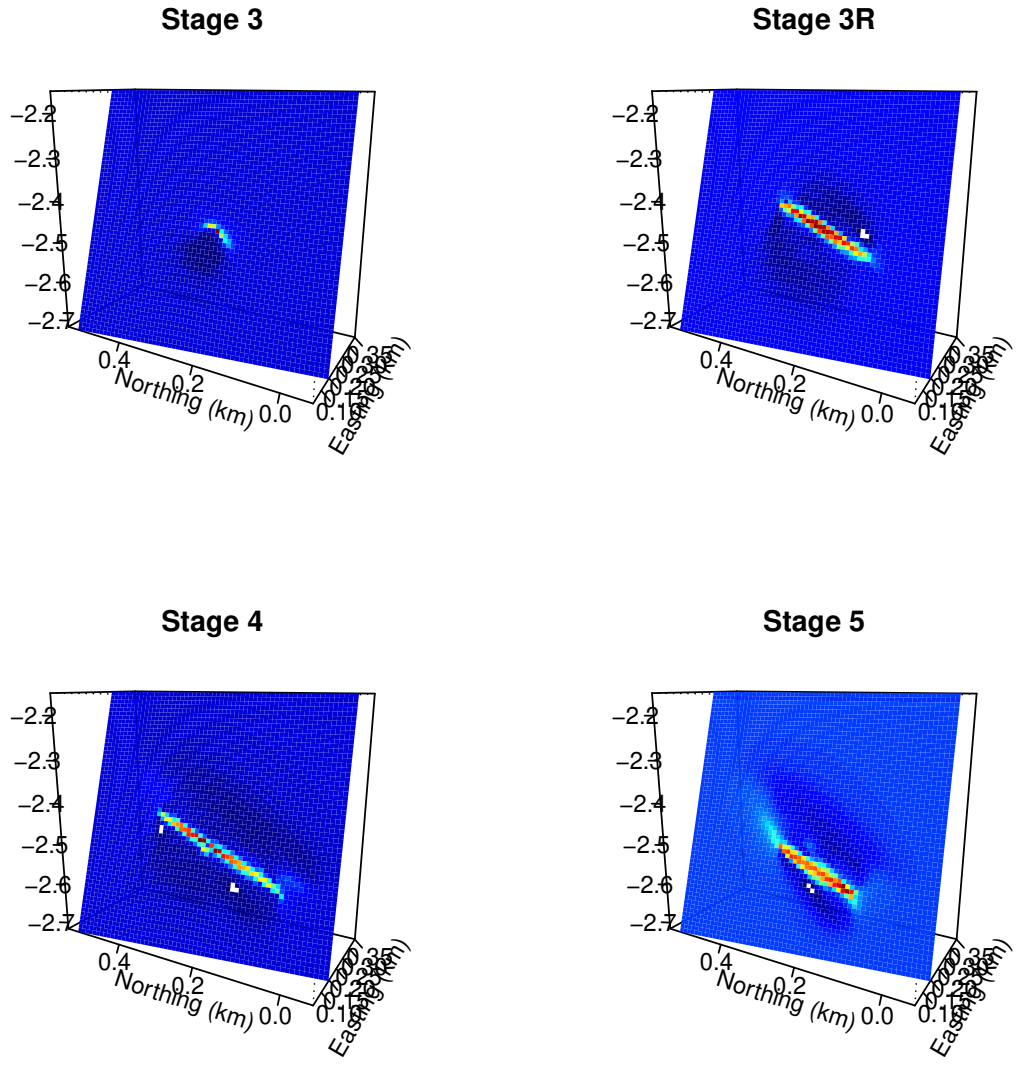

Figure 8: Visualization of the effective normal stress change due to each stimulation, projected onto the fracture surface at the time step that represents the average stress change across the entire stimulation. The effective normal stress change ranges from -32.9 MPa to -0.1 MPa across all four stimulations considered here. Normals stresses in RSQSim are reckoned positive in tension.

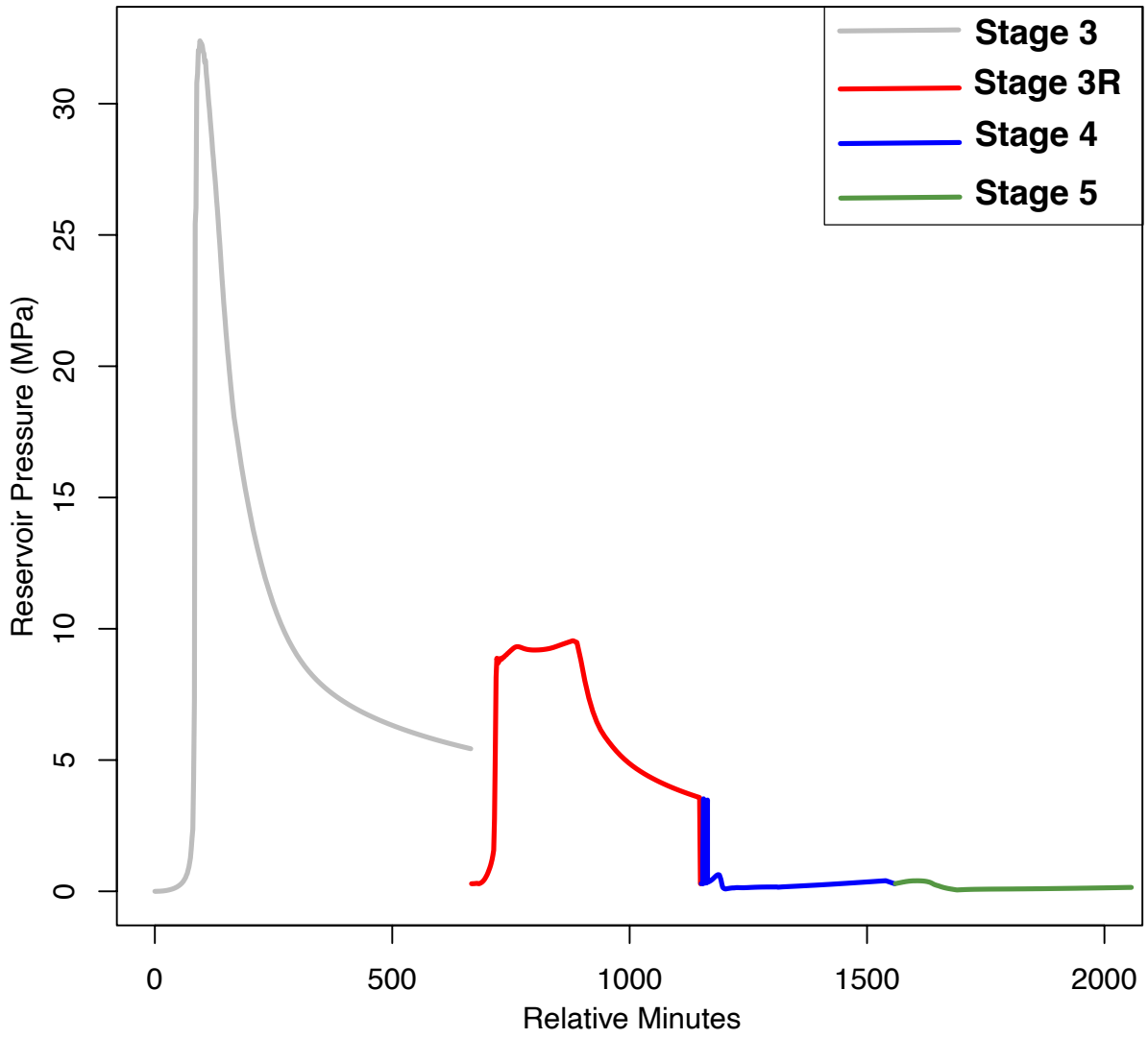

Figure 9: Time series of the effective normal stress changes (absolute value) for the element on the fracture that experiences the minimum normal stress change during each stage.

RSQSim Parameters	Values
Rate-State rate-coefficient, a,	0.004
Rate-State state-coefficient, b,	0.00533
Nominal coefficient of friction, μ	0.70
Characteristic slip distance, D_c, b	$9{\cdot}10^{-6}$ m
Reference velocity, V^*	$1{\cdot}10^{-6}$ m/sec
Slip velocity, V	1 m/sec
Rate-State normal stress dependency, α	0.05
Lamé Parameters, λ & μ	2400 GPa
Initial normal stress, σ	2 MPa
Initial state variable, θ,	$3.15{\cdot}10^{-7}$ sec

Table 3: Rate-state properties adopted in the RSQSim earthquake simulation.

4 THM+E Simulation Results of Stages 3-5

4.1 THM Simulation

Next, we present the simulation results for Stages 3–5, analyzing each stage individually. It is noted that the simulations for Stages 3R-5 use the setup shown in Figure 5b, which incorporates new DFN permeability to represent the stimulated region from Stage 3.

4.1.1 Stage 3

We begin with the Stage 3 THM simulation. Figure 10 shows the comparison between the pressure evolution predicted by the calibrated model and the field measurement, with the flow rate also shown for reference. As can be seen, with the calibrated $\alpha_k = 0.8$ MPa^{-1} and $k_{\max} = 10^{-7}$ m^2, the modeled pressure evolution aligns well with the field data, effectively capturing both the peak pressure and the slope of the pressure drop. Additionally, Figure 11 provides a side view (along the positive y-axis) of the pressure distribution around Stage 3 at different injection stages. It clearly illustrates the propagation of the stimulated region as injection progresses, while stimulation in the x-direction is not visible due to the anisotropic permeability specified in Eq. (2). Further, the stimulated zone from the THM simulation is compared with the spatial distribution of microseismic data for Stage 3 in Figure 12. The predicted stimulated region matches well with the microseismic data in terms of size and location. However, the microseismic data reveals upward growth of the stimulated region, likely due to the stress gradient, which is not captured by the current THM model. This discrepancy arises because the model assumes permeability enhancement is solely driven by pressure changes. Future work will incorporate stress dependency into the model to better replicate the observed hydraulic stimulation behavior.

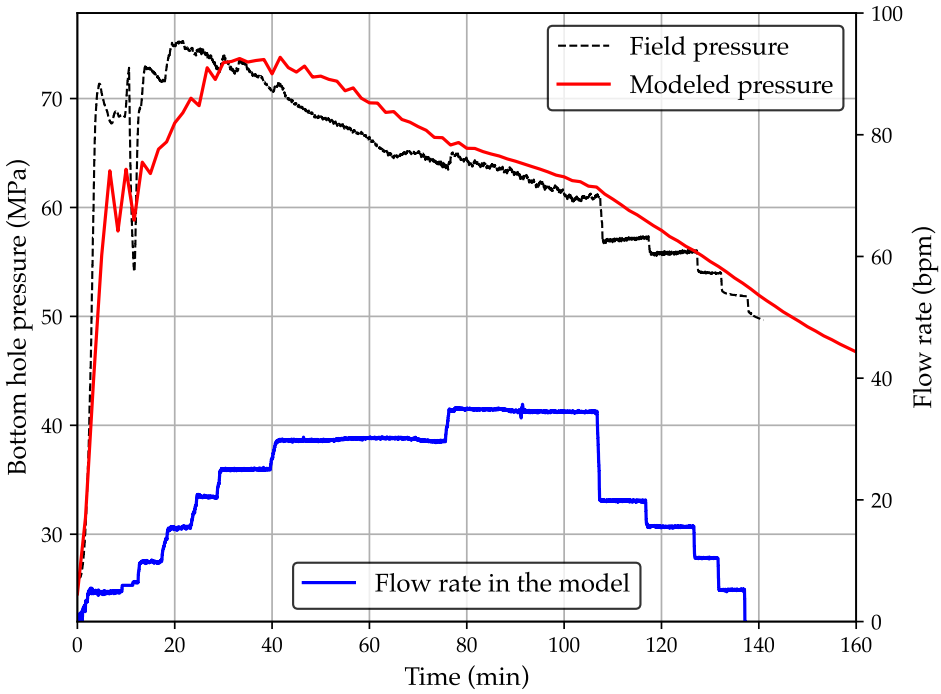

Figure 10: Comparison in the pressure evolution between the THM simulation and field data for Stage 3 stimulation.

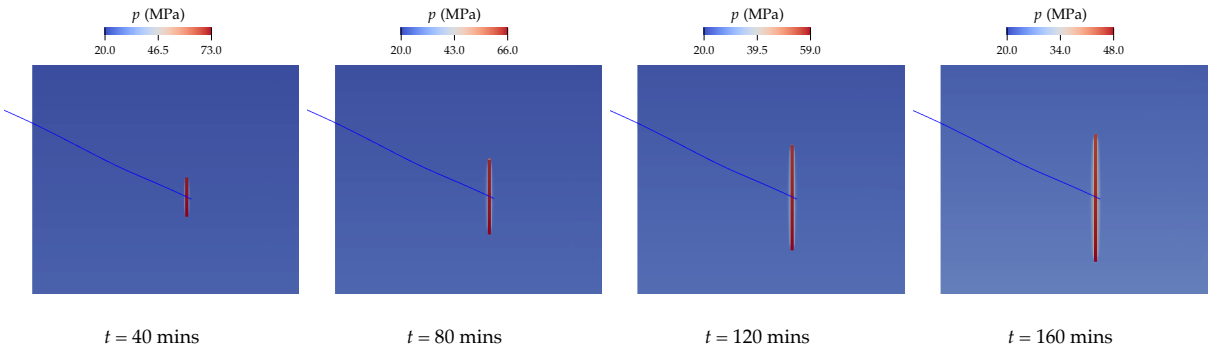

Figure 11: Pressure distribution for Stage 3 at different stages of injection.

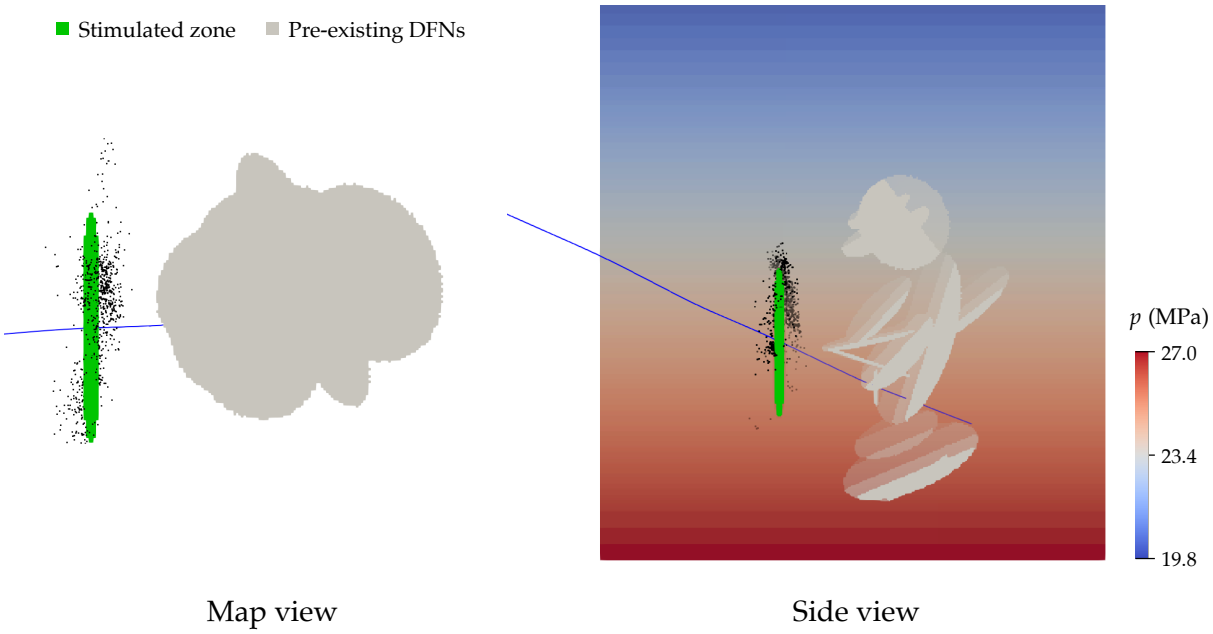

Figure 12: Comparison between the stimulated region from the THM simulation and the spatial distribution of microseismic data for Stage 3.

4.1.2 Stage 3R

Stage 3R aimed to re-stimulate the zones previously treated during Stages 1-3 in 2021. For modeling simplicity, injection is applied only at the Stage 3 location, with the flow rate set to 30% of the total injection rate based on fluid partition measurements from the July 2023 circulation test. Figure 13 compares the field data with the modeled pressure evolution using calibrated parameters $\alpha_k = 1.2\,\text{MPa}^{-1}$ and $k_{\max} = 1.2 \times 10^{-13}\,\text{m}^2$. Compared to Stage 3, a larger α_k required indicates a faster permeability enhancement, supporting the hypothesis that Stage 3R was reactivating/reopening fractures generated during Stage 3. The maximum allowable permeability, however, is significantly lower in order to replicate the relatively high residual pressure observed in the field. Additionally, unlike the continuous pressure drop seen in Stage 3, the injection pressure in Stage 3R stays at a constant residual value after pressure drop. This difference could be attributed to the change of the injection fluid (crosslink gel in Stage 3 v.s. slickwater in Stage 3R) or the possibility that Stage 3R was actually reopening a preexisting fracture plus large leakoff. To study whether Stage 3R could indeed reactivate/reopen fractures from Stage 3, Figure 14 presents the spatial distribution of permeability and pressure during injection. As we can see, the stimulated region of Stage 3R coincides with the preexisting fracture plane for Stage 3 at the very beginning of injection. As injection proceeds, pressure moves along the Stage 3 plane and gradually diffuses into other fracture planes as the stimulated

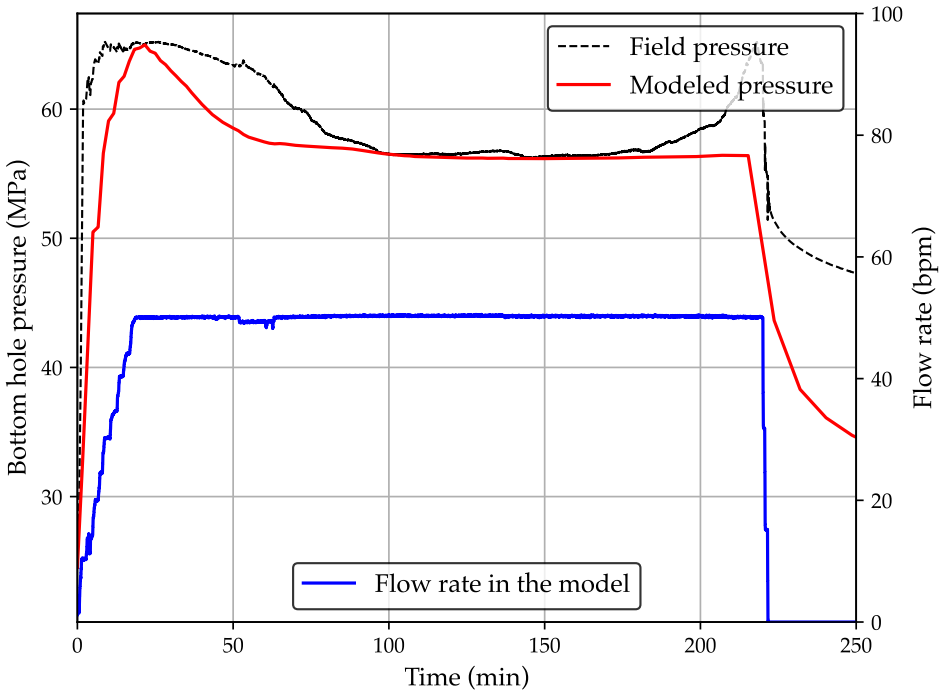

Figure 13: Comparison in the pressure evolution between the THM simulation and field data for Stage 3R stimulation.

region intersects with preexisting DFNs. By the end of injection, the pressure diffusion remains within the bounds of the preexisting fracture, indicating that no fracture propagation occurred during Stage 3R.

4.1.3 Stage 4

We then switch to the Stage 4 simulation. The modeled injection pressure from the THM simulation is compared with field data in Figure 15. With $\alpha_k = 3$ MPa^{-1} and $k_{\max} = 10^{-12}$ m^2, the simulation predicts an injection pressure that is generally consistent with the field measurement, particularly in terms of pressure dissipation and residual pressure. Notably, the calibrated parameters for the permeability model are slightly larger than those used for Stage 3 and 3R, suggesting that permeability enhancement becomes easier. This could be attributed to the re-stimulation of the reservoir by Stage 3R, especially considering the short interval of only a few hours between Stage 3R and Stage 4. Also, the fiber optics data indicate potential communication with Stage 3R (McClennan et al., 2024). To further investigate this inter-stage connectivity, we analyze the distribution of permeability and pressure at different injection stages, as shown in Figure 16. We can clearly see that the stimulated region grows with injection and

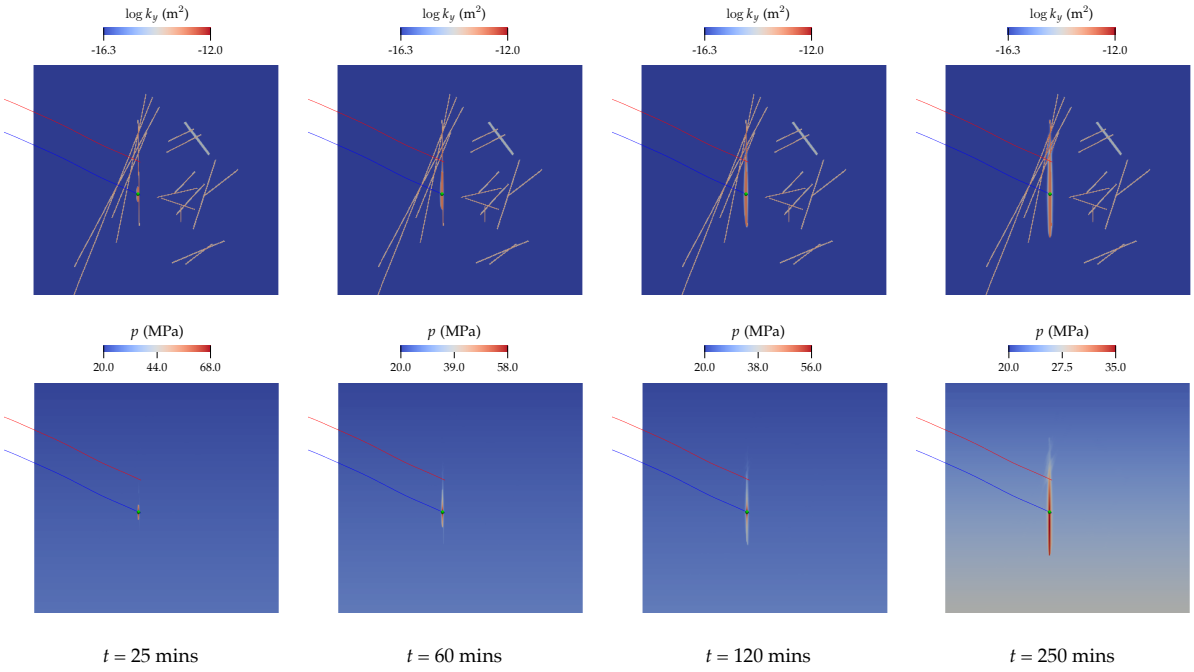

Figure 14: Distribution of permeability (upper row) and pressure (bottom row) for Stage 3R at different stages of injection. Wells 16A and 16B are shown in blue and red, respectively. The injection region is marked as a green circle.

gradually connects with DFN permeability at 40-60 mins, which coincides with the pressure drop seen in the injection curve. This suggests that the reduction in pressure is likely due to the intersection between the newly stimulated fractures and the pre-existing fractures. Additionally, the pressure diffusion during Stage 4 appears to branch as injection progresses, eventually connecting with the fracture plane associated with Stage 3 and Stage 3R on the right. This further supports the hypothesis of communication between Stages 4 and 3R.

4.1.4 Stage 5

Lastly, we present the simulation results for Stage 5. Figure 17 plots the modeled injection pressure using $\alpha_k = 0.6$ MPa^{-1} and $k_{\max} = 10^{-12}$ m^2. As can be seen, the modeling results well agree with the field data, showing a similar trend where the injection pressure decreases much more slowly compared to Stages 3R and 4. This slower pressure dissipation suggests limited permeability enhancement during Stage 5, which explains the need for a smaller α_k value in this case. The slower permeability enhancement could be attributed to the use of high-viscosity crosslinked gel in Stage 5 or the potential stress shadowing effect that constrains fracture growth and opening. Additionally, Stage 5 exhibits a lower peak pressure than the previous two stages. This might result from the Stage 5 fracture or stimulated region intersecting with preexisting

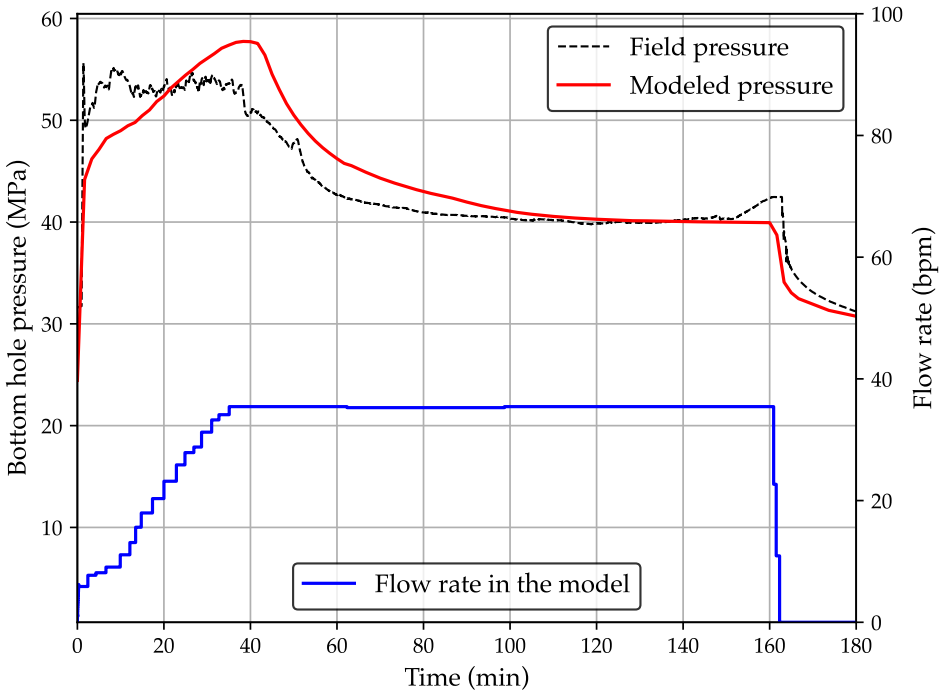

Figure 15: Comparison in the pressure evolution between the THM simulation and field data for Stage 4 stimulation.

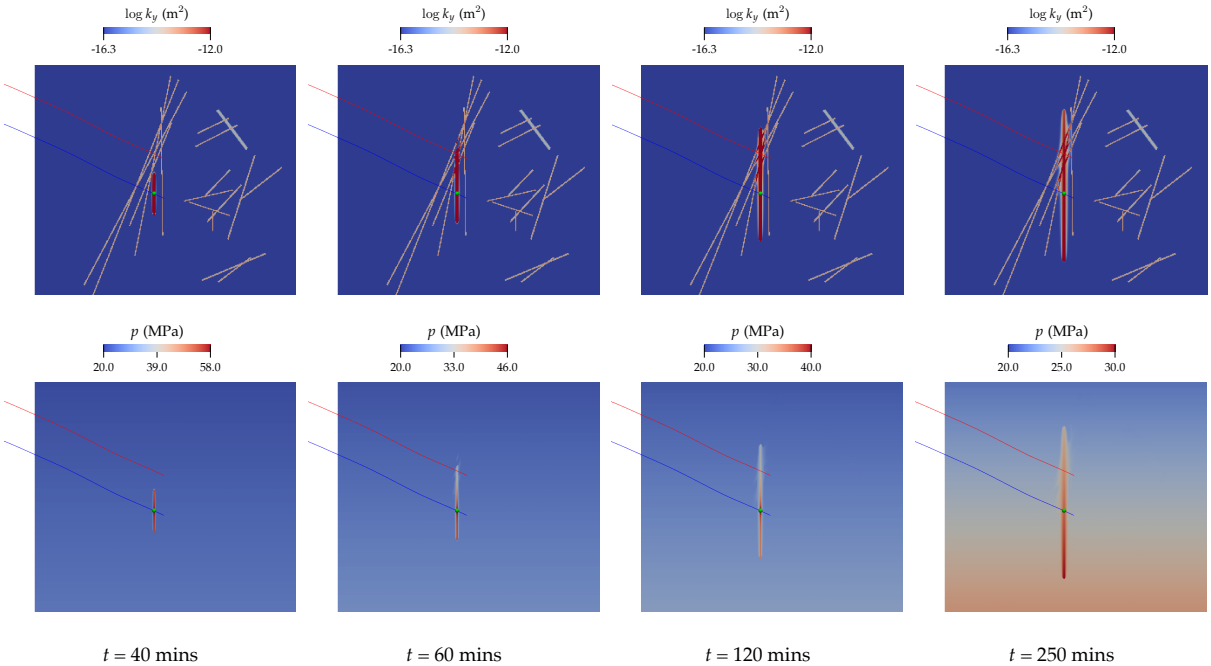

Figure 16: Distribution of permeability (upper row) and pressure (bottom row) for Stage 4 at different stages of injection. Wells 16A and 16B are shown in blue and red, respectively. The injection region is marked as a green circle.

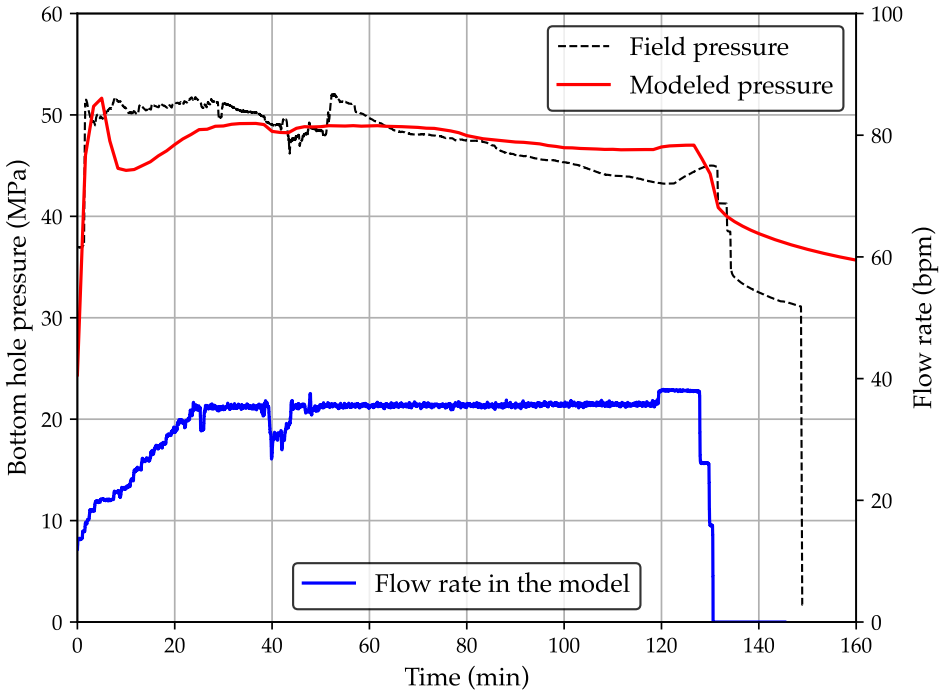

Figure 17: Comparison in the pressure evolution between the THM simulation and field data for Stage 5 stimulation.

DFNs immediately after injection begins, creating additional flow pathways and thereby reducing the injection pressure. This assumption also aligns with our main hypothesis that new stimulation stages (Stage 5 included) were reopening the previously stimulated region generated during Stage 3. To validate this assumption, Figure 18 presents the permeability and pressure distribution at four stages of injection. It clearly shows that the stimulated region intersects with preexisting DFNs as early as 10 minutes of the injection. This early intersection confirms our assumption that the lower peak pressure is likely caused by the rapid connection between the stimulated region and preexisting fractures.

4.2 THM+E Simulation of Stages 3-5

The pressure and stress history from all stimulations (Stage 3, 3R, 4, and 5) are concatenation and used to drive a single sinuation across all stages that preserves the time delay between Stage 3 and 3R. Because the earthquake simulations are deterministic and the spatial and temporal patterns of seismic activity arise from the complex interactions of fracture stress changes due to injection, slip during seismic events, material properties and frictional phenomena, it is impossible to predict the exact time and location of discrete events as they are observed. This makes activities

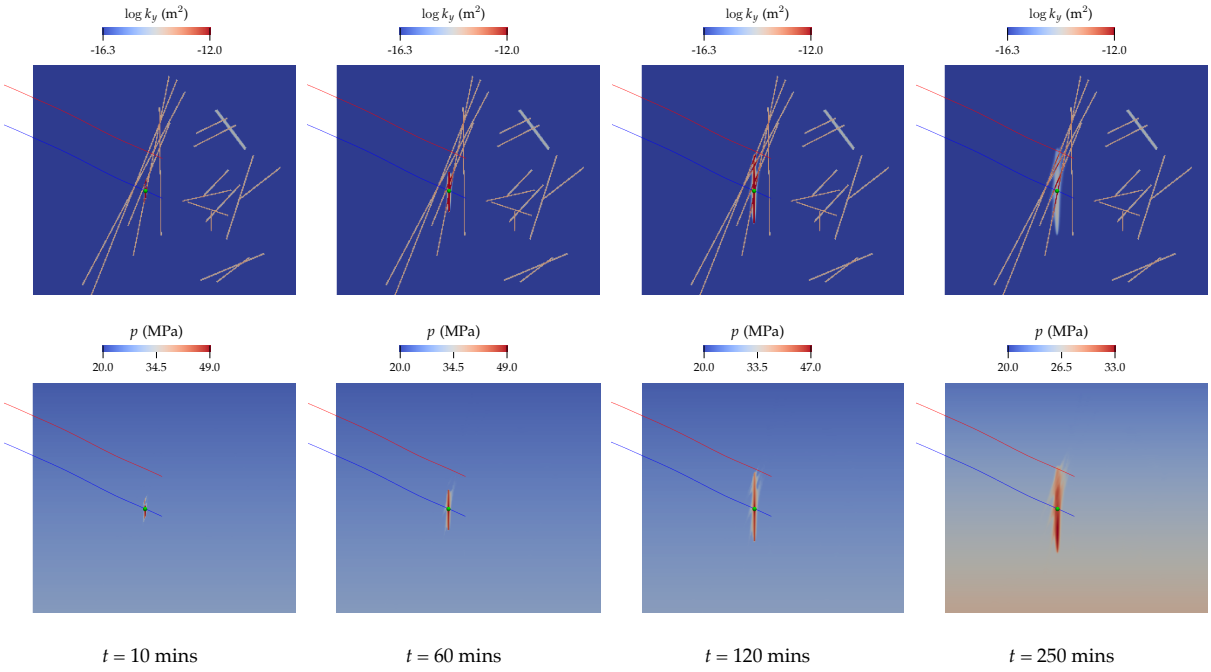

Figure 18: Distribution of permeability (upper row) and pressure (bottom row) for Stage 5 at different stages of injection. Wells 16A and 16B are shown in blue and red, respectively. The injection region is marked as a green circle.

such as "history matching" as is commonly performed in the reservoir engineering community impossible. Therefore, instead of matching the time history and spatial evolution of individual events, we focus our validation exercise on the ability of the simulations to match catalog-wide properties and statistics such as the range of event magnitudes, event rates, and the spatio temporal evolution of event locations.

Figures 19 and 20 compare the cumulative number of events that occurred in the simulation to those that were observed in the field. Event magnitudes for both event types are reported for to M≥ -1.5 for stage 3 and M≥0 for the remaining stages. The cutoff for Stage 3 is related to the magnitude of completeness of the catalog for that stage, where are magnitudes were only review for events with M≥0 for the latter stages. Events in Stage 3 are limited to those that occur prior to 300 minutes after the start of injection. This decision was made to address the fact that these simulations consider only a single fracture plane and do not consider the splay fracture that is activated >400 minutes after Stage 3 stimulation. In general, we see that the simulations do a very good job at capturing the overall event rates and the onset timing of seismic events in Stages 3, 4, and 5. However, the latter two simulations tend to produce more events in total for these stages. Conversely, relatively few events are produced in the Stage 3R simulation.

Figure 21 compares the distribution of event magnitudes between the simulations and the

observed events during each stage. The simulated event magnitudes are in good agreement for Stage 3, 3R, and 4, however the simulated events tend to be a bit larger in Stage 5 compared to the observed events. These larger magnitude events may be causing excess static stress changes that trigger subsequent aftershocks which may be driving the total number of events up as we showed in Figure 19(bottom right).

Figure 22 compares the location of all observed and simulated events (colored by stage) for three perpendicular "look" directions. Events tend to be clustered by stage, but generally migrate in similar directions in both cases. To explore the spatiotemporal evolution further, Figure 23 shows the distance between each event and the location of the injection stage. Here, the time gap between Stage 3 and Stage 3R is removed. We see good agreement between the simulate event migration and that of the observed events. Moreover, we also plot three diffusion curves to illustrate the expected moveout of events if the seismic activity were being induced by three flow regimes: pure matrix flow (dashed and dotted line), pure fracture flow (dashed line), and a dual permeability model of fracture and matrix flow (solid line). If the seismic events were responding to pure matrix flow, that would indicate that no fracture was generated and fluids were migrating directly through the pore-space in the rock unit. If the seismic events were responding to pure fracture flow, that would indicate a sustained/propped, relatively large aperture fracture. Neither pure matrix flow nor pure fracture flow models seem to explain the moveout of simulated or observed seismic events. Instead, in the event that a previously generated fracture experienced some, but not complete closure resulting in small aperture and some asperity contact, the moveout of seismic events might be expected to obey a moveout with a diffusivity indicative of a dual permeability model with contribtions from matrix flow and fracture flow. The latter case is observed of both the simulated and observed events.

5 Conclusions and Future Plans

Results shown here from THM+E simulations of the Stage 3, 3R, 4, and 5 stimulations, coupled with the observed DAS data seem to support the hypothesis that the original Stage 3 stimulation generated a new fracture, however, subsequent stimulations seemed only to propagate that existing Stage 3 fracture rather than generating new fractures of their own. If the alternative hypothesis were true, namely that four individual fractures were generated, we would not expect the simulation results to match the observations as well as they do. There are notable differences in the simulation results, particularly with regard to the lack of events during stage 3R that must be addressed. This artifact potentially arises due to the fact that there are quite a few events during Stage 3 at large distances from the injection point that are potentially due to

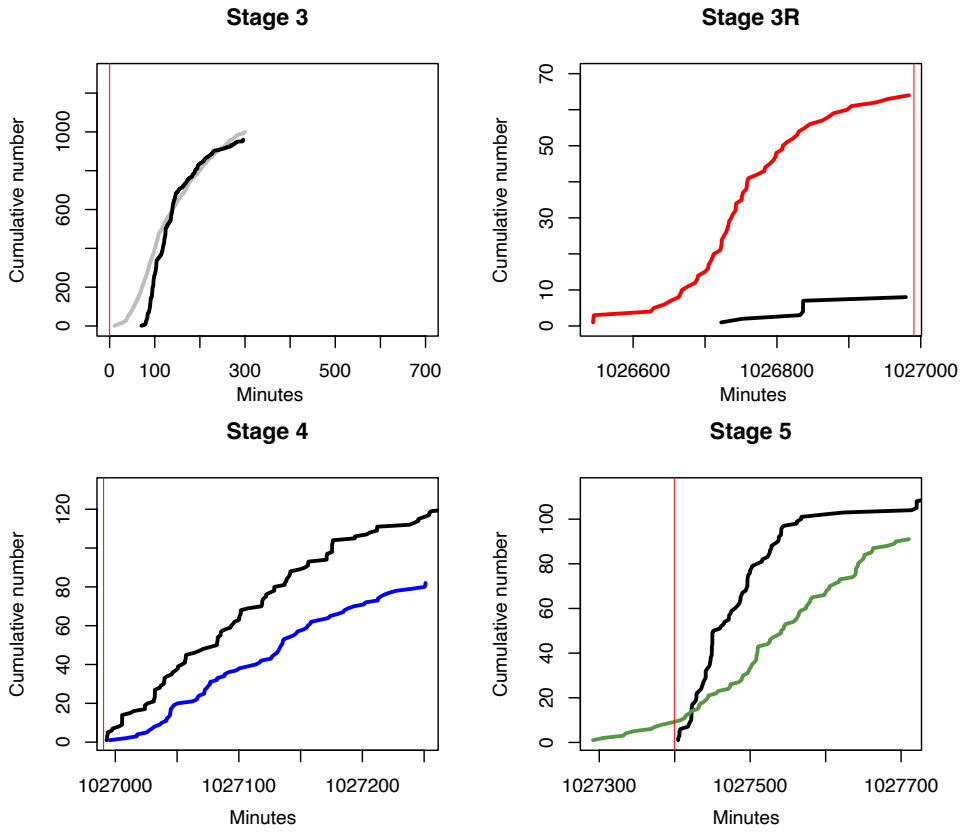

Figure 19: Comparison of the cumulative number of events that occur in the simulation (black) and the observed number of events that occur in the field during each stimulation.

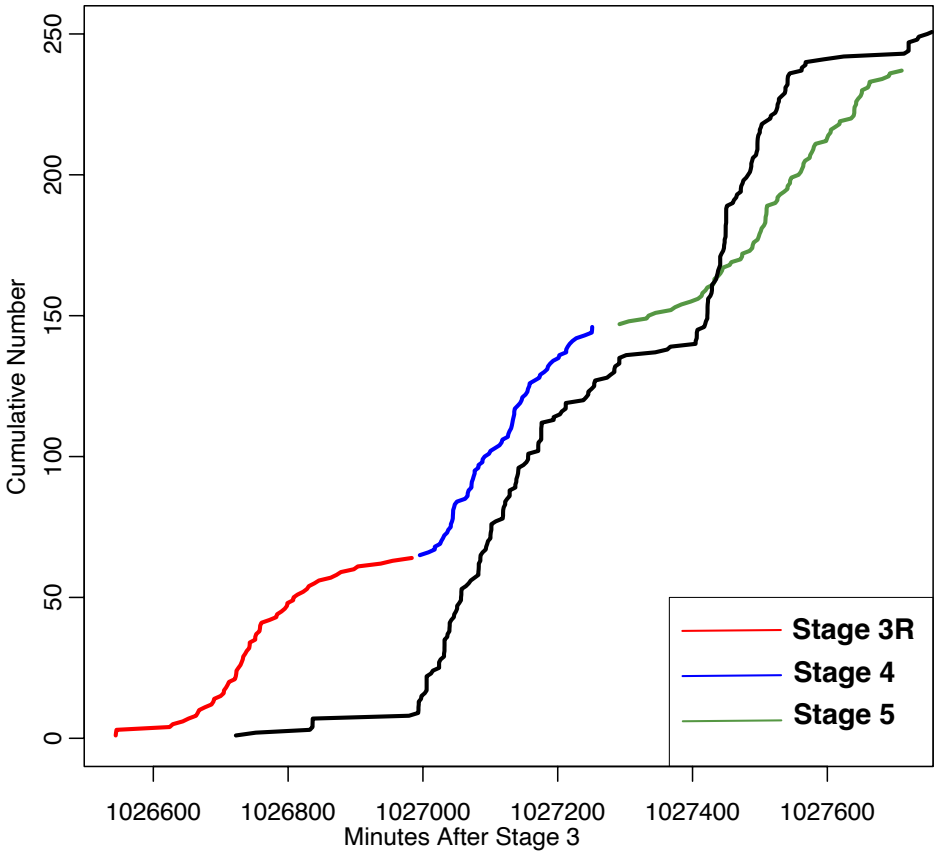

Figure 20: Stacked plot of the cumulative number of observed events for stages 3R, 4, and 5 (color) and simulated events (black), showing a decent agreement between the simulations and observations.

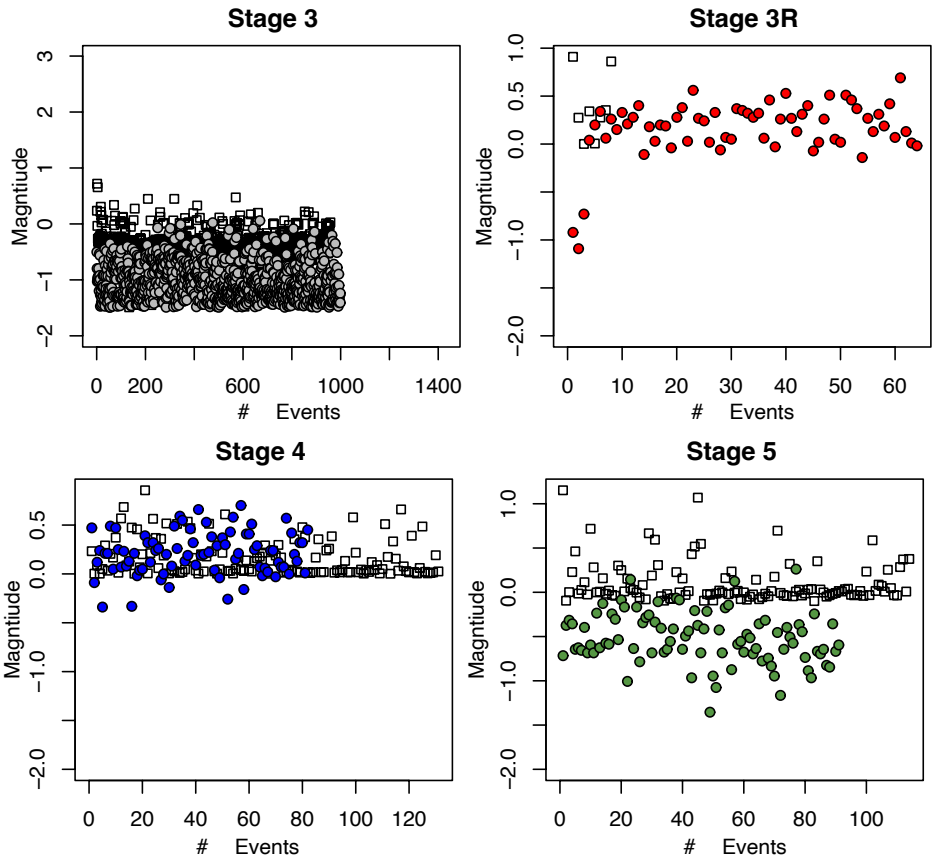

Figure 21: Comparison of the event magnitude and number of events for each stage. The simulated events are in black open squares and the observed events for each stage are in colored circles.

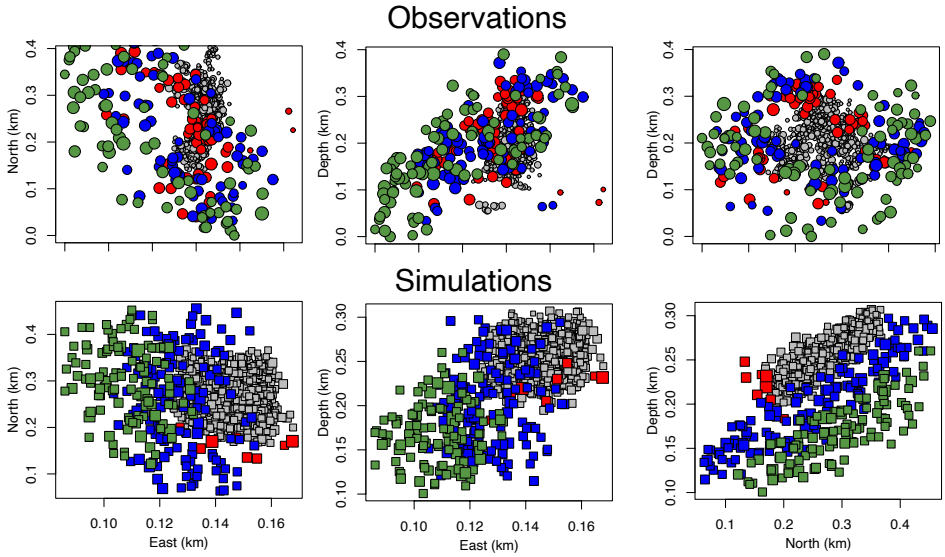

Figure 22: Comparison spatial distribution of observed events (top row) and the simulated events (bottom row). The color indicates the stage the events are associated with: Stage 3 (grey), Stage 3R (red), Stage 4 (blue), Stage 5 (green).

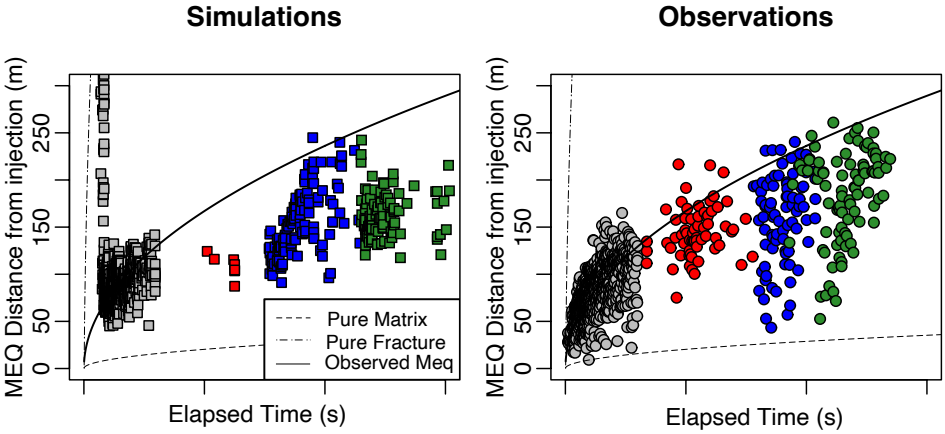

Figure 23: Comparison of the distance between each event and the injection point for the simulation events (left) and observed events (right) with color representing the stage (as in Figure 22. Curves show the projected moveout of seismic events away from the injection point in time, assuming three flow regimes: pure matrix flow (dashed and dotted line), pure fracture flow (dashed line), and a dual permeability model of fracture and matrix flow (solid line).

stress interactions, which may indicate that the initial shear stress state is too high. This will be corrected in year three of this project.

Future work related to these efforts will include the following:

1. Correcting the artifacts in the simulations with respect to Stage 3R.
2. Application of the THM pressure/stress conditions to a statistically significant number of realizations of the pre-existing shear stress field and/or application to fractures with geometric complexity to investigate the uncertainty in the simulations.
3. Completing the same set of simulations for Stages 6+ in well 16A and extending these simulations to include fractures that intersect with well 16B.
4. Complete circulation modeling to understand fluid and/or heat production capacity by circulating fluids between 16A and 16B.
5. Investigate the propensity for aseismic slip to occur under these conditions.

REFERENCES

Brune, N., J. (1970). Tectonic stress and the spectra of seismic shear waves from earthquakes. *Journal of Geophysical Research*, *75*(26), 4997–5009. Retrieved from `http://dx.doi.org/10.1029/JB075i026p04997` doi: 10.1029/JB075i026p04997

Dieterich, H., J. (1979). Modeling of rock friction, 1. Experimental results and constitutive equations. *J. Geophys. Res.*, *84*, 2161-2169.

Dieterich, J. H., & Richards-Dinger, K. B. (2010). Earthquake recurrence in simulated fault systems. In *Seismogenesis and earthquake forecasting: The frank evison volume ii* (pp. 233–250). Springer.

Dieterich, J. H., Richards-Dinger, K. B., & Kroll, K. A. (2015). Modeling injection-induced seismicity with the physics-based earthquake simulator rsqsim. *Seismological Research Letters*, *86*(4), 1102–1109.

Goff, J. A., & Jordan, T. H. (1989). Stochastic modeling of seafloor morphology: a parameterized gaussian model. *Geophysical Research Letters*, *16*(1), 45–48.

Graves, R., & Pitarka, A. (2016). Kinematic ground-motion simulations on rough faults including effects of 3d stochastic velocity perturbations. *Bulletin of the Seismological Society of America*, *106*(5), 2136–2153.

Haffener, J., Haustveit, K., & Ingle, T. (2022). Did we break new rock? utilizing diagnostics to differentiate new fracture creation vs old fracture reactivation: A meramec and wolfcamp study. In *Spe hydraulic fracturing technology conference and exhibition* (p. D021S006R002).

Jin, G., & Roy, B. (2017). Hydraulic-fracture geometry characterization using low-frequency das signal. *The Leading Edge*, *36*(12), 975–980.

Jurick, D., Guzik, A., Dyer, B., Meier, P., & Karvounis, D. (2024, 04). *Utah forge: Stimulation crosswell strain response fiber optic monitoring report - april 2024*. Retrieved from `https://gdr.openei.org/submissions/1686`

Kroll, K. A., Richards-Dinger, K. B., & Dieterich, J. H. (2017). Sensitivity of induced seismic sequences to rate-and-state frictional processes. *Journal of Geophysical Research: Solid Earth*, *122*(12), 10–207.

Lee, S. H., & Ghassemi, A. (2023). Modeling and analysis of stimulation and fluid flow in the utah forge reservoir. In *Proceedings: 48th workshop on geothermal reservoir engineering, stanford university, stanford, california.*

Linker, M. F., & Dieterich, H., James. (1992). Effects of variable normal stress on rock friction: Observations and constitutive equations. *J. Geophys. Res.*, *97*, 4923-4940.

Mai, P. M., & Beroza, G. C. (2002). A spatial random field model to characterize complexity in earthquake slip. *Journal of Geophysical Research: Solid Earth*, *107*(B11), ESE–10.

McClennan, J., Swearingen, L., & England, K. (2024, 11). *Utah forge: Wells 16a(78)-32 and 16b(78)-32 stimulation program report - may 2024*. Retrieved from `https://gdr.openei.org/submissions/1695` doi: 10.15121/2483880

Morrow, C., & Lockner, D. (1994). Permeability differences between surface-derived and deep drillhole core samples. *Geophysical Research Letters*, *21*(19), 2151–2154.

Nathenson, M. (1999). The dependence of permeability on effective stress from flow tests at hot dry rock reservoirs at rosemanowes (cornwall) and fenton hill (new mexico). *Geothermics*, *28*(3), 315–340.

Richards-Dinger, K., & Dieterich, J. H. (2012). Rsqsim earthquake simulator. *Seismological Research Letters*, *83*(6), 983–990.

Ruina, A. (1983). Slip instability and state variable friction laws. *Journal of Geophysical Research: Solid Earth*, *88*(B12), 10359–10370. Retrieved from `http://dx.doi.org/10.1029/JB088iB12p10359` doi: 10.1029/JB088iB12p10359

Ruina, L., A. (1980). *Friction laws and instabilities: A quasistatic analysis of some dry friction behavior*. Brown University. (PhD Dissertation)

Wang, C., Eaton, D. W., & Ma, Y. (2023). Numerical modeling of low-frequency distributed

acoustic sensing signals for mixed-mode reactivation. *Geophysics*, *88*(6), WC25–WC36.